

# IONIZATION AND DUST CHARGING IN PROTOPLANETARY DISKS

A.V. IVLEV<sup>1</sup>, V.V. AKIMKIN<sup>2</sup>, P. CASELLI<sup>1</sup>

<sup>1</sup>Max-Planck-Institut für Extraterrestrische Physik, Giessenbachstr. 1, 85748 Garching, Germany and  
<sup>2</sup>Institute of Astronomy of the Russian Academy of Sciences, Pyatnitskaya St. 48, 119017 Moscow, Russia

*Draft version June 16, 2019*

## ABSTRACT

Ionization-recombination balance in dense interstellar and circumstellar environments is a key factor for a variety of important physical processes, such as chemical reactions, dust charging and coagulation, coupling of the gas with magnetic field and the development of magnetorotational instability in protoplanetary disks. We present a self-consistent analytical model which allows us to exactly calculate abundances of charged species in dusty gas, in the regime where the dust-phase recombination dominates over the gas-phase recombination. The model is employed to verify applicability of a conventional approximation of low dust charges in protoplanetary disks, and to discuss the implications for the dust coagulation and the development of the “dead zone” in the disk. Furthermore, the importance of mutually consistent models for the ionization and dust evolution is addressed: These processes are coupled via several mechanisms operating in the disk, and therefore their interplay can be crucial for the ultimate dust evolution and the formation of macroscopic bodies.

*Subject headings:* ISM: dust – protoplanetary disks – ISM: clouds – ISM: cosmic rays – astrochemistry

## 1. INTRODUCTION

An accurate calculation of ionization-recombination balance in dense protoplanetary conditions is essential for understanding various fundamental problems, such as coupling of the gas with magnetic field (Li et al. 2014), accretion processes (Turner et al. 2014), chemistry (Semenov et al. 2004; Larsson et al. 2012) and dust evolution (Okuzumi et al. 2011b; Akimkin 2015). Both the ionization and recombination processes can arise from several sources. While the treatment of ionization, despite the variety of ionization sources, could be reduced to a single (total) ionization rate, the description of recombination is less straightforward. At sufficiently high densities, the dominant sink of free electrons and ions are dust grains, and the recombination rate non-trivially depends on properties of the grains. Furthermore, accretion of electrons and ions leads to non-zero grain charges, which effectively changes the grain-grain (Okuzumi 2009) and gas-grain (Weingartner & Draine 1999) interactions as well as the grain dynamics.

Depletion of electrons caused by the presence of dust grains significantly reduces the degree of ionization in dense interstellar conditions (Umebayashi 1983; Umebayashi & Nakano 1990; Nishi et al. 1991): In comparison with dust-free gas, the electron-to-ion ratio may drop by as much as a square root of the effective ion-to-electron mass ratio (which is a factor of 74 for a plasma with dominant  $H_3^+$  ions, or 231 for  $N_2H^+/HCO^+$  ions). As the ionization controls the coupling of the gas to the magnetic field, and hence the development of the magnetorotational instability (MRI, e.g., Velikhov 1959; Balbus & Hawley 1991), dust is the essential ingredient for any MRI model. It has been shown that the grain size critically affects the size of a disk’s “dead zone” (Sano et al. 2000; Bai 2011a,b; Dodorov & Khaibrakhmanov 2014). Nevertheless, anal-

ysis of MRI has been usually carried out assuming properties of dust are fixed.

In dense protoplanetary environments, the coagulation of sub- $\mu m$  interstellar dust particles becomes an important process. The planet formation in protoplanetary disks requires the dust to form larger and larger aggregates, until gravitational forces become dominant (e.g., Testi et al. 2014, and references therein). There is a clear evidence of grain growth to millimeter and centimeter sizes within protoplanetary disks (e.g., Pérez et al. 2015; van der Marel et al. 2015). However, significant difficulties are found during this coagulation process, such as bouncing barriers (e.g., Zsom et al. 2010) and particle fragmentation (Birnstiel et al. 2012) after initial grain compaction and growth. Many theoretical and laboratory studies have greatly advanced our understanding of grain growth and planetesimal formation in recent years (Dominik et al. 2007; Johansen et al. 2014, and references therein), with particular attention dedicated to dust traps, now detected with ALMA toward protoplanetary disks (van der Marel et al. 2013, 2015; Pinilla et al. 2015; Zhang et al. 2016). In dust traps, particles are expected to grow more easily due to the locally enhanced dust-to-gas mass ratio (Booth & Clarke 2016; Surville et al. 2016), although the details of this coagulation process are far from being understood, considering the largely unknown dust properties.

As has been already pointed out, the ionization does not only determine dynamical and chemical processes occurring in protoplanetary disks, but also leads to the dust charging and thus affects the coagulation. Collisions with electrons and ions lead to (on average) negative grain charges due to higher electron velocities. Recently, it has been shown that the coagulation of larger aggregates in protoplanetary disks can be inhibited due to growing Coulomb repulsion between them – the resulting electrostatic potential barrier is roughly proportional to the aggregate size (Okuzumi 2009; Okuzumi et al. 2011a,b). Along with the plasma charging, other charging mecha-

nisms can operate in protoplanetary disks. In Akimkin (2015) the photoelectric emission from grains, induced by stellar radiation and leading to their positive charging, was considered as a mechanism to overcome the electrostatic barrier in upper disk regions. A similar mechanism – photoelectric charging due to  $\text{H}_2$  fluorescence induced by cosmic rays (CRs) – operates in much deeper regions at the disk periphery (Ivlev et al. 2015). However, both mechanisms become negligible in dense regions of the disk. We notice that the (still poorly investigated) effect of charging on the dust evolution has recently received increased interest (Carballido et al. 2016).

In this paper, we present an analytical model which becomes exact in sufficiently dense astrophysical environments and allows us to self-consistently calculate densities of the charged species, in particular – to obtain the dust charges for arbitrary grain size distributions. As the average charge of grains scales linearly with their size (typically, above  $\sim 1 \mu\text{m}$ ), we utilize the model to verify whether the broadly used approximation of low grain charges is valid for sufficiently evolved dust. We also discuss the importance of self-consistent analysis of the ionization and the grain evolution, as these processes are mutually coupled via several mechanisms operating in the disks. Our analytical model has only one free parameter (the effective mass of the ions), and can be easily included in numerical simulations following the dust evolution in dense molecular clouds and protoplanetary disks.

The paper is organized as follows. In Section 2 we consider the overall ionization-recombination balance and introduce a recombination threshold – the gas density above which the electron-ion recombination is dominated by the processes on the dust surface. In Section 3 we present the grain charge distribution determined by accretion of electrons and ions, and point out important limiting cases of “big” and “small” grains. In Section 4 we derive the governing equations for the dust-phase recombination regime, complemented with the grain charge distribution, which allow us to calculate densities of the charged species in a general form; to reveal generic properties of the solution, we consider “monodisperse” dust (grains of the same size) and investigate separately the limits of “big” and “small” grains. The effect of the grain size distribution is studied in Section 5. We discuss implications of the proposed model for protoplanetary disks in Section 6, and summarize the results in Section 7.

## 2. DUST-PHASE RECOMBINATION REGIME

The ionization-recombination balance for electrons is generally governed by the following equation:

$$\zeta n_g = R_g + R_d, \quad (1)$$

where  $\zeta$  is the total ionization rate<sup>1</sup> of gas with the number density  $n_g$ . The recombination is represented by the two terms:  $R_g = \sum_k \beta_g^{(k)} n_e n_i^{(k)}$  describes the gas-phase recombination of electrons and ions, where  $\beta_g^{(k)}$  is the rate of recombination with the  $k$ th ion species

<sup>1</sup> The magnitude of  $\zeta$  is determined by a combination of different ionization mechanisms (due to CRs, X-rays, UV, and radionuclides) whose relative importance varies across the disk (e.g., Armitage 2015).

(with the density  $n_i^{(k)}$ , the summation is over all ion species), while  $R_d = \beta_d n_e n_d$  is the electron collection flux on dust (in equilibrium it is equal to the collection flux of all ion species). The respective recombination rate  $\beta_d = 2\sqrt{2\pi} a^2 v_e e^{-\Psi}$  (where  $v_e = \sqrt{k_B T/m_e}$  is the thermal velocity scale for electrons) is determined by the normalized floating potential  $\Psi = |\langle Z \rangle| e^2 / a k_B T$  of a grain of radius  $a$  (Fortov et al. 2005). Dust comprises a small mass fraction of gas,

$$m_d n_d = f_d m_g n_g, \quad (2)$$

where  $m_g \simeq 2.3 m_p$  is the mean mass of gas particles (expressed in units of the proton mass  $m_p$ ), and the fraction  $f_d$  is of the order of  $10^{-2}$  in the interstellar medium. Thus, the dust density  $n_d$  is proportional to  $n_g$ .

To evaluate the relative contribution of the two recombination terms, one can set  $n_e = \sum_k n_i^{(k)}$  (this is verified in Section 4.1). Equations (1) and (2) suggest that for sufficiently low  $n_g$  the gas-phase recombination is the dominant process (i.e.,  $R_d$  is negligible), and  $n_e$  varies with the gas density as  $\propto \sqrt{\zeta n_g}$ .<sup>2</sup> At higher  $n_g$  the situation is reversed: By solving Equation (1) for  $n_e$  we conclude that, when the gas density exceeds a *dust-phase recombination threshold*,<sup>3</sup>

$$n_g \gtrsim n_g^{\text{rec}} = \frac{\zeta \beta_g (m_d/m_g)^2}{2\pi f_d^2 v_e^2 a^4} e^{2\Psi}, \quad (3)$$

(where  $\beta_g$  is the characteristic gas-phase recombination rate), the electron/ion density is primarily determined by the recombination on grains. By substituting typical values  $\zeta \sim 10^{-17} \text{ s}^{-1}$  and  $T \sim 10^2 \text{ K}$ , and taking into account that  $\beta_g \lesssim 10^{-7} \text{ cm}^3 \text{ s}^{-1}$  (e.g., Okuzumi 2009), for micron-size grains we obtain that the gas-phase recombination in a heavy-ion  $\text{HCO}^+/\text{N}_2\text{H}^+$  plasma ( $\Psi = 3.86$ ) is negligible for  $n_g \gg n_g^{\text{rec}} \sim 10^9 \text{ cm}^{-3}$ ; for a  $\text{H}_3^+$  plasma ( $\Psi = 2.94$ ) the recombination threshold is an order of magnitude lower. We note that the characteristic recombination rate  $\beta_g$  depends on details of the gas-phase reactions (Oppenheimer & Dalgarno 1974), and therefore generally the value of  $n_g^{\text{rec}}$  is known only approximately.

Thus, for  $n_g \gg n_g^{\text{rec}}$  – below we call this the *dust-phase recombination regime* – the ionization degree is (practically) not affected by a variety of reactions occurring in the gas phase. The emergence of this regime reflects the growing importance of dust in the global ionization-recombination balance. It is noteworthy that if the grain size polydispersity is taken into account, then (depending on the particular shape of the size distribution) the value of  $n_g^{\text{rec}}$  can be decreased significantly (see Section 5). As regards the effect of the grain morphology, this can also be straightforwardly included by assuming a certain dependence of the grain mass on size, e.g., by adopting a fractal scaling law  $m_d \propto a^D$  with some appropriate dimensionality  $D \leq 3$ . However, given a large uncertainty

<sup>2</sup> When  $R_g$  includes both the dissociative recombination and the radiative recombination with heavy metal ions, the scaling for  $n_e$  may change between  $\propto (\zeta n_g)^{1/3}$  and  $\propto \zeta n_g$ , depending on the density of metals and the magnitude of  $\zeta$ . Such a behavior is typical for different regions of molecular clouds (e.g., Oppenheimer & Dalgarno 1974).

<sup>3</sup> The recombination threshold is defined as the gas density at which  $R_g(n_g) = R_d(n_g)$ .

in the dependence  $m_d(a)$ , we leave this discussion for a separate paper.

### 3. GRAIN CHARGE DISTRIBUTION

A stationary discrete charge distribution  $N(Z, a) \equiv N_Z$  is obtained from the detailed equilibrium of the charging master equation (Draine & Sutin 1987; Draine 2011), and is presented in Appendix B. The charge distribution, derived for dust grains of a given size  $a$  and normalized to the total differential dust density at that size,

$$\sum_Z N_Z = dn_d(a)/da, \quad (4)$$

depends on two dimensionless numbers (Draine & Sutin 1987; Ivlev et al. 2015): The effective ion-to-electron mass ratio  $\tilde{m}$ , determined by the partial contributions of all ions and characterized by the effective atomic mass of ions  $A$  (in amu), and the normalized potential of the unit charge  $\tilde{\varphi}$  (or, equivalently, the inverse reduced temperature):

$$\frac{\tilde{m}}{1836} = \left( \sum_k \frac{1}{\sqrt{A_k}} \frac{n_i^{(k)}}{n_e} \right)^{-2} \equiv A \left( \frac{n_e}{n_i} \right)^2, \quad (5)$$

$$\tilde{\varphi} = \frac{e^2}{ak_B T} = \frac{1.67}{(a/0.1 \mu\text{m})(T/100 \text{ K})}, \quad (6)$$

where  $n_i \equiv \sum_k n_i^{(k)}$  is the total ion density and  $A_k$  is the atomic mass number of the  $k$ th ion species. While  $\tilde{\varphi}$  can, in principle, be arbitrary small (big grains or/and high temperatures) or large, the value of  $\tilde{m}$  has well-defined upper and lower bounds: As long as dust does not noticeably affect the overall charge balance,  $n_e \simeq n_i$ , we have  $\tilde{m} \simeq 1836A$ . When the contribution of the negatively charged dust becomes crucial,  $n_e \ll n_i$ , one can show (see Section 4) that  $\tilde{m}$  asymptotically tends to unity (i.e.,  $n_e/n_i$  tends to a small constant of  $1/\sqrt{1836A}$ ), in order to satisfy the charge neutrality.

From Equations (B2) and (B3) we obtain the charge distribution for two limiting cases: Irrespective of the magnitude of  $\tilde{m}$ , for  $\tilde{\varphi} \ll 1$  the charge distribution tends to a Gaussian form (Draine & Sutin 1987),

$$\tilde{\varphi} \ll 1: \quad N_Z \propto e^{-(Z-\langle Z \rangle)^2/2\sigma_Z^2}, \quad (7)$$

the average charge  $\langle Z \rangle = -\tilde{\varphi}^{-1}\Psi$  and the charge variance  $\sigma_Z^2 = \tilde{\varphi}^{-1}(1+\Psi)/(2+\Psi)$  are determined by the normalized potential  $\Psi$ , which is the solution of the charging equation,

$$(1 + \Psi)e^\Psi = \sqrt{\tilde{m}}. \quad (8)$$

For  $\tilde{\varphi} \gg 1$  the distribution is essentially discrete – the singly-charged states are

$$\tilde{\varphi} \gg 1: \quad \frac{N_{\pm 1}}{N_0} \simeq \frac{\tilde{m}^{\mp 1/2}}{\tilde{\varphi}}, \quad (9)$$

i.e., grains with  $Z = -1$  are the most abundant; the states with  $|Z| \geq 2$  are usually exponentially small and practically negligible. In Section 4.2 we discuss the role of the polarization interactions on the charge distribution (Draine & Sutin 1987), neglected in our consideration, and also identify conditions where the multiply charged states become important (Section 6.2).

### 4. DENSITIES OF CHARGED SPECIES

In the dust-phase recombination regime, the self-consistent ionization degree and the grain charge distribution are determined by a set of two equations: the ionization-recombination balance equation and the charge-neutrality equation.

We start with the derivation of the ionization-recombination equation. The equilibrium charge distribution discussed above is determined by the detailed balance of the electron and ion fluxes on a grain surface, and therefore it does not matter which of these fluxes is used to calculate the recombination. For convenience, we consider the ion collection term, which can be presented in the following general form:

$$R_d = 2\sqrt{2\pi} v_i n_i \int da a^2 \mathcal{N}(a), \quad (10)$$

where  $v_i = \sqrt{k_B T / Am_p}$  is the effective thermal velocity scale of ions and  $\mathcal{N}(a)$  is the effective number density of grains of radius  $a$ , obtained for the ion collection in Appendix C. By substituting  $\mathcal{N}(a)$  from Equation (C1), we derive the equation

$$\begin{aligned} \zeta n_g &= 2\sqrt{2\pi} v_i n_i \\ &\times \sum_{Z \geq 0} (\sqrt{\tilde{m}} + \tilde{m}^{-Z}) \int da a^2 e^{-Z\tilde{\varphi}} N_{-Z}. \end{aligned} \quad (11)$$

Note that the summation is performed over *non-positive* charge states.

Next, we obtain the charge-neutrality equation. The charge density of dust grains (of a given size) is  $\sum_Z Z N_Z$ , where summation over the positive-charge states can be eliminated by using Equation (B2). Then the integration over the size distribution yields

$$n_i - n_e = \sum_{Z > 0} (1 - \tilde{m}^{-Z}) \int da Z N_{-Z}, \quad (12)$$

where the summation is over *negative* charge states.

Equations (11) and (12) are complemented with the normalization condition for the dust density, Equation (4). Again, by eliminating summation over the positive-charge states we obtain

$$N_0 + \sum_{Z > 0} (1 + \tilde{m}^{-Z}) N_{-Z} = dn_d(a)/da. \quad (13)$$

The derived set of governing Equations (11)–(13), along with the relation  $\tilde{m} = 1836A(n_e/n_i)^2$  and Equation (B3), allows us to calculate self-consistent charge distributions for arbitrary grain-size distributions, and obtain the corresponding electron and (total) ion densities. The gas density  $n_g$  and the ionization rate  $\zeta$ , which is generally a decreasing function of  $n_g$ , are the input parameters for the derived model. The effective atomic mass of the ions  $A$  is the only free parameter (entering through the effective mass ratio  $\tilde{m}$  and the velocity scale  $v_i \propto 1/\sqrt{A}$ ). The model is *exact* as long as the gas-phase recombination plays no role, i.e., when the strong condition (3) is satisfied.

A detailed analysis of the governing equations and their solutions is presented in Sections 4.1 and 4.2. Now we

TABLE 1  
NOTATIONS USED IN THE ARTICLE.

Symbol	Meaning
$A$	effective atomic mass of ions [amu]
$a$	dust grain radius [cm]
$f_d$	dust-to-gas mass ratio
$m_g, m_d, m_e, m_p$	mass of a gas particle, dust grain (of radius $a$ ), electron, and proton [g]
$\tilde{m}$	effective ion-to-electron mass ratio
$N_Z \equiv N(Z, a)$	discrete charge distribution of grains of radius $a$ [cm <sup>-4</sup> ]
$dn_d(a)/da$	differential size distribution of grains [cm <sup>-4</sup> ]
$n_g, n_e, n_i$	number density of gas particles, electrons, and the total number density of ions [cm <sup>-3</sup> ]
$n_{EI}$	number density of an electron-ion (EI) plasma [cm <sup>-3</sup> ]
$n_g^{\text{rec}}$	recombination threshold, separating the gas-phase and dust-phase recombination regimes [cm <sup>-3</sup> ]
$n_g^{\text{dep}}$	electron depletion threshold, at the transition to a dust-ion (DI) plasma [cm <sup>-3</sup> ]
$n_g^{\text{asy}}$	asymptotic threshold, at the transition to a dust-dust (DD) plasma [cm <sup>-3</sup> ]
$R_g, R_d$	gas-phase and dust-phase recombination rates [cm <sup>-3</sup> s <sup>-1</sup> ]
$T$	gas/dust temperature (same for all species) [K]
$v_e, v_i, v_d$	thermal velocity scale of electrons, ions (of the atomic mass $A$ ), and grains (of radius $a$ ) [cm s <sup>-1</sup> ]
$Z, \langle Z \rangle$	grain charge state and average charge number
$\beta_g$	characteristic rate coefficient for the gas-phase recombination [cm <sup>3</sup> s <sup>-1</sup> ]
$\beta_d$	rate coefficient for the dust-phase recombination [cm <sup>3</sup> s <sup>-1</sup> ]
$\zeta$	total ionization rate [s <sup>-1</sup> ]
$\tilde{\varphi}$	normalized grain potential for the unit charge
$\Psi = \langle Z \rangle \tilde{\varphi}$	normalized grain potential for charge number $\langle Z \rangle$ (limiting case $\tilde{\varphi} \ll 1$ )

would like to point out an important generic relation between the electron-to-ion density ratio and the gas density, which can be inferred from Equations (11) and (12): Given  $dn_d/da \propto n_g$ , the ionization-recombination equation yields  $n_i(n_g) \propto \zeta$ . One of the main contribution to the ionization in protoplanetary disks is provided by interstellar CRs. Their attenuation at a given location is determined by the *least* gas column density along the propagation paths (the total intensity of CRs is obtained by integrating over all directions of propagation, assuming interstellar CRs to be isotropic, Padovani et al. 2009; Ivlev et al. 2015). Since  $n_g$  increases along such “shortest” paths, while  $\zeta$  is a decreasing function of the column density, we conclude that  $n_i$  decreases with  $n_g$ . Thus, the electron-ion contribution to the charge neutrality, the lhs of Equation (12), falls off, while the dust contribution, the integral on the rhs, increases linearly with  $n_g$ . As long as the dust contribution is negligible, viz.,  $n_g$  is much smaller than a certain threshold  $n_g^{\text{dep}}$  (to be defined in Section 4.1 – but, of course,  $n_g \gg n_g^{\text{rec}}$  is assumed), the charge neutrality is reduced to  $n_i - n_e \simeq 0$ . For  $n_g \gtrsim n_g^{\text{dep}}$ , however, Equation (12) can only be satisfied if  $\tilde{m} \propto (n_e/n_i)^2$  decreases with  $n_g$ ; asymptotically,  $n_e/n_i$  should approach a small value of  $1/\sqrt{1836A}$ , to ensure  $\tilde{m} \rightarrow 1$ , and the average grain charge tends to zero as  $|\langle Z \rangle| \propto \tilde{m} - 1 \propto \zeta/n_g$ .

In the following Sections we study separately the two limiting cases of  $\tilde{\varphi} \ll 1$  and  $\tilde{\varphi} \gg 1$ . The former case corresponds to the most interesting situations when grains grow well beyond several microns and/or the ambient gas temperature becomes of the order of  $\sim 100$  K – such conditions are at best matched in the inner midplane region of the disk (Armitage 2007). We also study the opposite limit, corresponding to low temperatures of  $\lesssim 30$  K and/or small grains with  $a \lesssim 0.1 \mu\text{m}$ . This case describes dust at the initial coagulation stage in the outer disk regions, where the gas density is nevertheless high enough to satisfy condition (3).

To clearly identify the role of different physical effects,

in Sections 4.1 and 4.2 we first assume that all grains have the same size (then the integration in Equations (11) and (12) is removed, and  $dn_d/da$  in Equation (13) is replaced with the total dust density  $n_d$ ), and discuss generic effects introduced by the size polydispersity in Section 5. For convenience, in Table 1 we summarize the main notations used throughout the paper.

#### 4.1. Case $\tilde{\varphi} \ll 1$ (big grains/high temperature)

The charge distribution in this case is described by a broad Gaussian function, Equation (7), so the summation over  $Z$  can be replaced with the integration. Let us elaborate on how densities of the charged species vary with  $n_g$ .

As discussed above, as long as the gas density is below a certain threshold  $n_g^{\text{dep}}$ , the charge neutrality is governed by electrons and ions,  $n_e \simeq n_i$ , i.e., we are dealing with an *electron-ion* (EI) plasma; the effective mass ratio in this case,  $\tilde{m} = \tilde{m}_{EI} (\simeq 1836A)$ , does not depend on  $n_g$ . The corresponding potential  $\Psi_{EI}$ , derived from Equation (8), is about a few (e.g., Fortov et al. 2005), and therefore the average charge  $|\langle Z_{EI} \rangle| = \tilde{\varphi}^{-1} \Psi_{EI}$  is much larger than the charge dispersion  $\simeq \tilde{\varphi}^{-1/2}$ . Thus, the charge distribution can be well approximated by a shifted delta function,  $N_Z \propto n_d \delta(Z - \langle Z \rangle)$ . Let us assume that this approximation is also applicable for  $n_g \gtrsim n_g^{\text{dep}}$  (as demonstrated below in this Section). By substituting the delta-function in Equations (11) and (12), employing Equation (8), and neglecting small terms  $\tilde{m}^{-|\langle Z \rangle|}$ , we reduce the governing equations to the following form:

$$\zeta n_g = 2\sqrt{2\pi} v_i n_i (1 + \Psi) a^2 n_d, \quad (14)$$

$$n_i - n_e = \Psi \tilde{\varphi}^{-1} n_d, \quad (15)$$

where the dust and gas densities are related by Equation (2). These equations are solved together with the charging Equation (8). The presented approach is equivalent to that used by Okuzumi (2009).

Now we can determine the *electron depletion threshold*  $n_g^{\text{dep}}$ . We define this as  $n_g$  at which the dust charge



density, given by the rhs of Equation (15), becomes equal to the electron density.<sup>4</sup> This yields

$$\left(\frac{n_g}{\zeta}\right)_{\text{dep}} = \frac{(m_d/m_g)^2}{4\sqrt{2\pi}f_d^2v_1a^2} \frac{\tilde{\varphi}}{\Psi_{\text{EI}}(1 + \Psi_{\text{EI}})}. \quad (16)$$

Above we pointed out that  $\zeta(n_g)$  is a non-increasing function, and therefore the lhs of Equation (16),  $(n_g/\zeta)_{\text{dep}} \equiv n_g^{\text{dep}}/\zeta(n_g^{\text{dep}})$ , is a single-valued (increasing) function of  $n_g^{\text{dep}}$ . To obtain the magnitude of  $n_g^{\text{dep}}$ , we set for simplicity  $\zeta = \text{const}$  and assume typical values used to estimate  $n_g^{\text{rec}}$  from Equation (3); for  $\tilde{\varphi} \sim 0.03$  we have  $n_g^{\text{dep}} \sim 10^3 n_g^{\text{rec}}$ . We notice that (for  $\zeta = \text{const}$ ) the ratio  $n_g^{\text{dep}}/n_g^{\text{rec}} \propto a/\sqrt{AT}$  is a rather weak function of the temperature and atomic mass. Generally, both  $n_g^{\text{dep}}$  and  $n_g^{\text{rec}}$  should be obtained from  $n_g/\zeta(n_g)$ .

The density of electrons (ions) at  $n_g \lesssim n_g^{\text{dep}}$ , denoted as  $n_{\text{EI}}(n_g)$ , is directly obtained from Equation (14) with  $\Psi = \Psi_{\text{EI}}$ . This can be expressed in terms of  $(n_g/\zeta)_{\text{dep}}$  as

$$\frac{n_{\text{EI}}}{\zeta} = 2f_d \frac{m_g}{m_d} \frac{\Psi_{\text{EI}}}{\tilde{\varphi}} \left(\frac{n_g}{\zeta}\right)_{\text{dep}}, \quad (17)$$

i.e., the ratio  $n_{\text{EI}}/\zeta$  does not depend on  $n_g$  (note that it is also independent of  $\tilde{\varphi}$ ). Equation (17) represents the density of a “regular” EI plasma, where dust still does not affect the charge neutrality. Simultaneously, this equation provides a convenient normalization for the electron and ion densities at  $n_g \gtrsim n_g^{\text{dep}}$ , where a crossover to a *dust-ion* (DI) plasma occurs: The charge neutrality in this case is regulated by positive ions and negatively charged dust grains, so the total ion density  $n_i$  and the potential  $\Psi$  can be approximately calculated by neglecting  $n_e$  in Equation (15). Together with Equations (14), (16) and (17), this leads to the following simple relations for  $n_g \gtrsim n_g^{\text{dep}}$ :

$$\frac{\Psi(1 + \Psi)}{\Psi_{\text{EI}}(1 + \Psi_{\text{EI}})} \simeq \frac{(n_g/\zeta)_{\text{dep}}}{(n_g/\zeta)}, \quad (18)$$

$$\frac{n_i}{n_{\text{EI}}} \simeq \frac{1 + \Psi_{\text{EI}}}{1 + \Psi}. \quad (19)$$

To derive  $n_i(n_g)$ , one has to substitute  $\Psi(n_g)$  from Equation (18) and  $n_{\text{EI}}(n_g)$  from Equation (17) in Equation (19). The electron density  $n_e$  is obtained by substituting  $n_i$  in Equation (8), and noting that  $\sqrt{m} = (n_e/n_i)\sqrt{m_{\text{EI}}}$ . This yields

$$\frac{n_e}{n_{\text{EI}}} \simeq e^{-(\Psi_{\text{EI}} - \Psi)}. \quad (20)$$

Equations (18)–(20) show that, in a DI plasma,  $\Psi$  and hence the average charge  $| \langle Z \rangle | = \tilde{\varphi}^{-1}\Psi$  monotonically decrease with  $n_g$  and, when  $\Psi \lesssim 1$ , tend to the asymptotic dependence  $\Psi(n_g) \propto \zeta/n_g$ , as expected. Correspondingly, the asymptotic ion density  $n_i(n_g)$  is a factor of  $1 + \Psi_{\text{EI}}$  times  $n_{\text{EI}}(n_g)$ . The density ratio  $n_e/n_i$  approaches the predicted small value  $1/\sqrt{m_{\text{EI}}}$ .

<sup>4</sup> Mathematically, this is equivalent to the condition that the total ion density  $n_i$ , obtained from Equation (14), is two times the dust charge density.

Remarkably, relations (18)–(20) remain valid even when the magnitude of the average charge becomes smaller than the charge dispersion,<sup>5</sup>  $| \langle Z \rangle | \lesssim \sigma_Z$ , which is equivalent to  $\Psi \lesssim \sqrt{\tilde{\varphi}}$ . Using Equation (18), we obtain that this occurs when  $n_g$  exceeds another characteristic density, the *asymptotic threshold*  $n_g^{\text{asy}}$ , determined by

$$\left(\frac{n_g}{\zeta}\right)_{\text{asy}} = \frac{\Psi_{\text{EI}}(1 + \Psi_{\text{EI}})}{\sqrt{\tilde{\varphi}}} \left(\frac{n_g}{\zeta}\right)_{\text{dep}}. \quad (21)$$

Equation (21) identifies the next important crossover, now from a DI to a *dust-dust* (DD) plasma: For  $n_g \gtrsim n_g^{\text{asy}}$ , the charge neutrality is increasingly dominated by a balance between negatively and positively charged grains. Thus, both transitions (at  $n_g^{\text{dep}}$  and  $n_g^{\text{asy}}$ ) are a manifestation of the growing importance of dust in the overall charge balance.

The charge dispersion in Equation (7) remains large at any gas density – for  $n_g \gg n_g^{\text{dep}}$  the variance tends to a constant large value,  $2\sigma_Z^2 \rightarrow \tilde{\varphi}^{-1}$ . The average charge keeps decreasing further, and for  $n_g/\zeta \gtrsim \tilde{\varphi}^{-1/2}(n/\zeta)_{\text{asy}}$  it becomes less than unity. Thus, the charge distribution asymptotically becomes quasi-symmetric with respect to  $Z = 0$ .

We see that the obtained results are completely characterized by  $n_{\text{EI}}$  and  $n_g^{\text{dep}}$ . These characteristic densities are functions of the effective atomic mass of ions  $A$ , which is the only free parameter of our model. The left panel in Figure 1 shows  $\Psi_{\text{EI}}$  as well as the asymptotic density ratio  $(n_i/n_e)_{\text{DD}}$ , both plotted versus  $A$ . In the right panel, functions representing the dependencies  $n_{\text{EI}}(A)$  and  $n_g^{\text{dep}}(A)$  are depicted (recall that  $v_1 \propto 1/\sqrt{A}$ ). In principle,  $A$  may vary between unity (hydrogen ions) and some large numbers (e.g., 56 for iron ions), but astrochemical models (Semenov et al. 2004) suggest that molecular and metal ions, such as  $\text{HCO}^+/\text{N}_2\text{H}^+$  ( $A = 29$ ) and  $\text{Mg}^+$  ( $A = 24$ ), usually dominate in very dense molecular clouds and protoplanetary disks. From Figure 1 we see that the uncertainty in  $n_{\text{EI}}$  and  $n_g^{\text{dep}}$ , associated with the plasma composition in this case, does not exceed a few dozens of percent. This effect is practically negligible next to uncertainties introduced by poorly known grain-size distribution (e.g., Kim et al. 1994; Weingartner & Draine 2001) and grain morphology (the latter determined dependence of the grain mass on its effective size).

Figure 2 summarizes the behavior of the average dust charge and of the electron and ion densities in the entire dust-phase recombination regime, and also illustrates modification of the dust charge distribution with increasing  $n_g$ . The densities are normalized by  $n_{\text{EI}}(n_g)$ , so for  $n_g \ll n_g^{\text{dep}}$  we have  $n_e/n_{\text{EI}} = n_i/n_{\text{EI}} = 1$ . The value of  $\Psi_{\text{EI}}$  weakly depends on the average atomic mass of ions  $A$  (the plotted curves are for  $\text{HCO}^+/\text{N}_2\text{H}^+$  ions). The solid red lines show the exact solution of the governing Equations (14) and (15) together with the charging Equation (8), which are equivalent to Equations (32)–(34) of Okuzumi (2009). With the used normalization, the

<sup>5</sup> In this case, a shifted delta-function is no longer a good approximation for Equation (7). Nevertheless, substituting the latter into Equations (11) and (12) (with neglected  $n_e$ ) leads to the relations derived above.

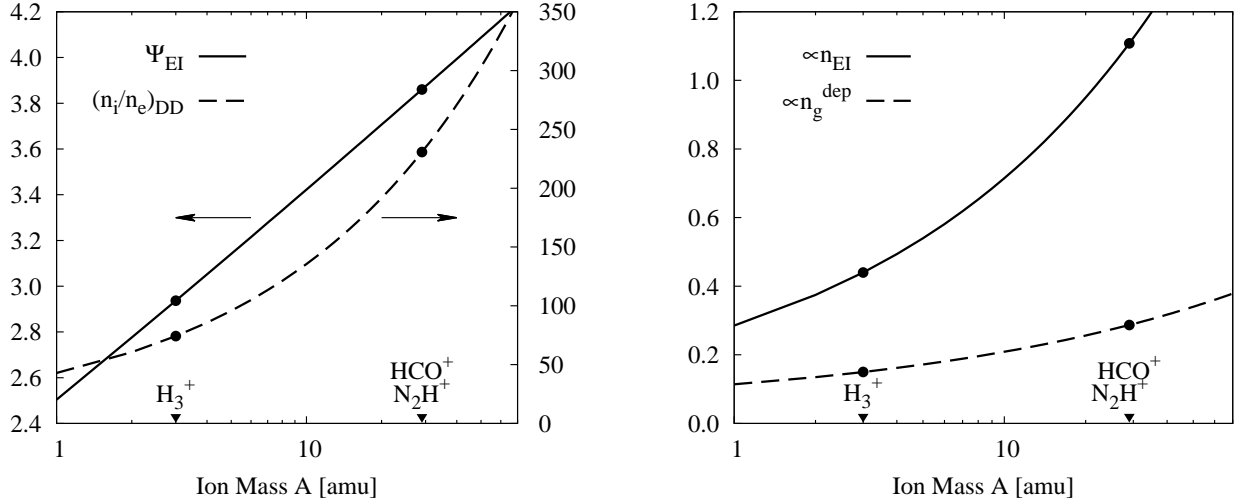


FIG. 1.— (Left) Potential of a grain in an electron-ion (EI) plasma,  $\Psi_{\text{EI}}$ , and the ion-to-electron density ratio in a dust-dust (DD) plasma,  $(n_i/n_e)_{\text{DD}}$ , plotted as functions of the effective atomic mass of ions  $A$ . (Right) Plots representing the EI plasma density,  $\sqrt{A} (1 + \Psi_{\text{EI}})^{-1} \propto n_{\text{EI}}(A)$ , and the electron depletion threshold,  $\sqrt{A} \Psi_{\text{EI}}^{-1} (1 + \Psi_{\text{EI}})^{-1} \propto n_g^{\text{dep}}(A)$ . In both panels, values for typical ions  $\text{H}_3^+$ ,  $\text{N}_2\text{H}^+$ ,  $\text{HCO}^+$  are indicated.

curves have a universal form, applicable for arbitrary set of parameters in the dust-phase recombination regime. The behavior at  $n_g \gtrsim n_g^{\text{dep}}$  is well reproduced by approximate relations (18)–(20), shown by the red dashed lines, with the maximum deviation at  $n_g = n_g^{\text{dep}}$  (where the ion density is underestimated by  $\simeq 20\%$ , while the grain potential and the electron density are overestimated by  $\simeq 30\%$  and a factor of  $\simeq 2.5$ , respectively). Note that  $\tilde{\varphi}$  is an arbitrary small parameter in the considered case, and therefore the point  $\Psi \sim \sqrt{\tilde{\varphi}}$  (which identifies the crossover to a DD plasma) could in principle be located below the shown asymptotic line  $n_e/n_{\text{EI}} = e^{-\Psi_{\text{EI}}}$ .

So far we have assumed that the gas temperature is constant. In protoplanetary disks, the relative temperature increase toward the center is usually not as strong as the increase of the gas density. Nevertheless, this is a noticeable effect which can in fact be straightforwardly incorporated in our model – the temperature simply becomes an additional input parameter. Moreover, it turns out that in many cases, for instance – in the disk mid-plane,  $T$  and  $n_g$  are related by a simple power-law dependence,  $T \propto n_g^\epsilon$  (e.g., with  $\epsilon = 2/11$ , see Armitage 2007). We notice that the gas temperature enters the thermal velocity  $v_i \propto \sqrt{T}$  and the normalized unit-charge potential  $\tilde{\varphi} \propto T^{-1}$ , thus affecting the electron depletion threshold  $n_g^{\text{dep}}$ . From this we immediately infer that the ratio  $(n_g/\zeta)_{\text{dep}}$  on the lhs of Equations (16) should be replaced with  $(n_g^{1+3\epsilon/2}/\zeta)_{\text{dep}}$  (then the rhs is properly normalized with the respective density scale entering the  $T \propto n_g^\epsilon$  dependence); both ratios on the rhs of Equation (18) are replaced in the same way. As regards  $n_{\text{EI}}$ , the lhs of Equation (17) should be multiplied with  $(n_g/n_g^{\text{dep}})^{\epsilon/2}$ , i.e.,  $n_{\text{EI}}$  falls off with gas density as  $\propto \zeta/n_g^{\epsilon/2}$ .

When considering recombination on grains, we have so far also implicitly assumed that only free electrons and ions contribute to this process. Such an approach is natural since the thermal velocities of plasma

species are much larger than typical thermal velocities of grains, and therefore the terms describing recombination due to mutual dust collisions (Umebayashi 1983; Umebayashi & Nakano 1990) are omitted in Equation (11). On the other hand, in a DD plasma grains become the most abundant charged species and, thus, collisions between them may provide an important contribution to the net recombination rate. This occurs when the product  $n_d v_d$  becomes comparable to the thermal ion flux  $n_i v_i$ , where  $v_d$  is the relevant (thermal or non-thermal) scale for the relative velocity of grains. By substituting the asymptotic expression for  $n_i(n_g)$  we conclude that the recombination mechanism due to mutual dust collisions should be important at  $n_g/\zeta \gtrsim (v_i/v_d)(n_g/\zeta)_{\text{dep}}$ . If the thermal motion dominates dust dynamics, the corresponding gas density exceeds  $n_g^{\text{dep}}$  by many orders of magnitudes: e.g., for micron-size grains in a  $\text{HCO}^+$  plasma,  $n_g$  should be of the order of  $3 \times 10^5 n_g^{\text{dep}}$  ( $\sim 10^4 n_g^{\text{asy}}$ ). However, the condition can be significantly relaxed for grains exhibiting strong non-thermal motion, e.g., due to differential drift or sedimentation (Testi et al. 2014). Furthermore, since  $(n_g/\zeta)_{\text{dep}} \propto f_d^{-2}$ , an increase of the dust fraction occurring due to various processes operating in the disk mid-plane (see Section 6.1) also promotes this mechanism of recombination.

#### 4.2. Case $\tilde{\varphi} \gg 1$ (small grains/low temperature)

In this case the charge distribution is practically limited by the singly-charged and neutral states, as it follows from Equation (9). By substituting the charge distribution in Equation (13) we derive

$$N_0 \simeq (1 + \sqrt{\tilde{m}}/\tilde{\varphi})^{-1} n_d, \quad (22)$$

$$N_{-1} \simeq (1 + \tilde{\varphi}/\sqrt{\tilde{m}})^{-1} n_d, \quad (23)$$

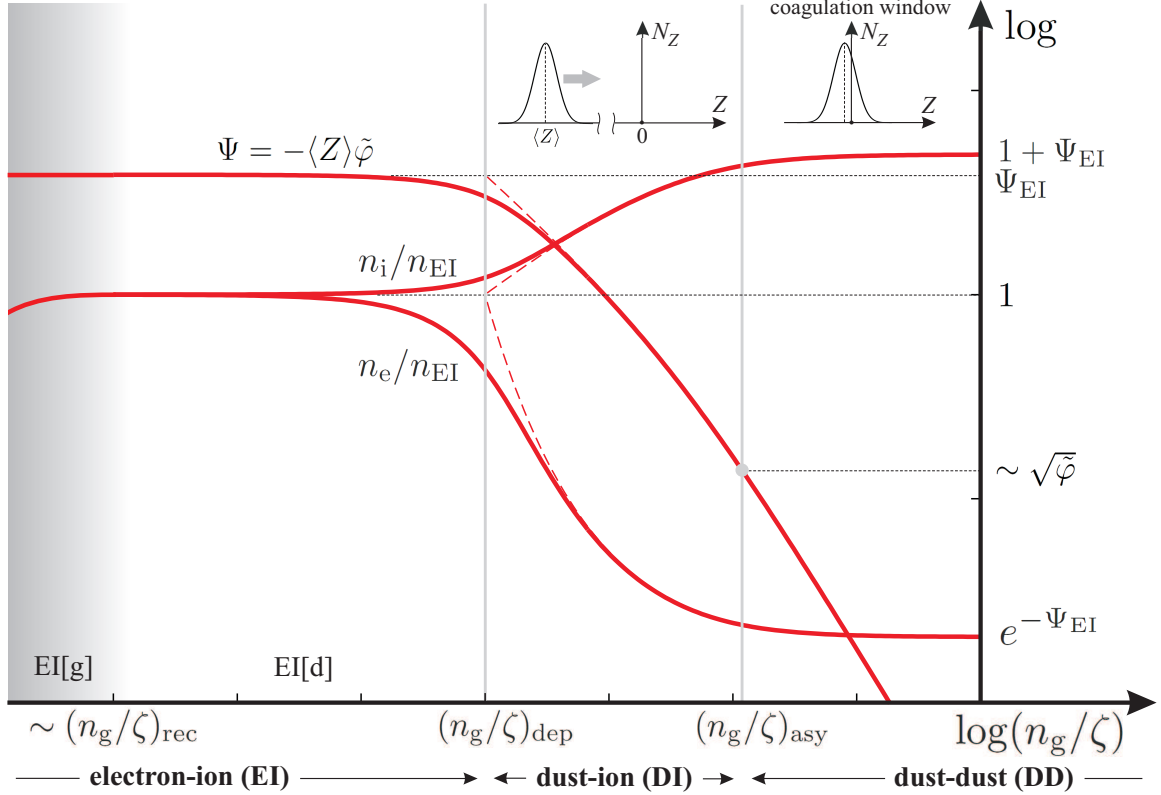


FIG. 2.— Universal behavior of charged species in the *dust-phase recombination regime*  $n_g \gtrsim n_g^{\text{rec}}$ , Equation (3): At these gas densities, the recombination of electrons and ions on dust grains dominates over their gas-phase recombination (a gradual transition occurring at  $n_g \sim n_g^{\text{rec}}$  is marked by the grey shading). The dust density is proportional to  $n_g$ , all shown parameters depend on  $n_g$  via the ratio  $n_g/\zeta(n_g)$  (the results are shown in a log-log scale, decades are indicated). The three characteristic ranges of  $n_g$  represent a “regular” electron-ion (EI) plasma with the gas-phase (EI[g]) and dust-phase (EI[d]) recombination, an “intermediate” dust-ion (DI) plasma, and a “high-density” dust-dust (DD) plasma. The red solid lines depict the normalized potential of a grain  $\Psi$ , proportional to the average dust charge  $\langle Z \rangle < 0$ , as well as the normalized electron density  $n_e$  and the total ion density  $n_i$ . In an EI plasma, electrons and ions have the same densities equal to  $n_{\text{EI}}(n_g)$ , Equation (17), the grain potential is constant and equal to  $\Psi_{\text{EI}}$ . A gradual crossover to a DI plasma occurs at the *electron depletion threshold*  $n_g \sim n_g^{\text{dep}}$ , Equation (16): The electron-to-ion density ratio  $n_e/n_i$  and hence  $\Psi$  start to decrease monotonically, so at larger  $n_g$  the charge neutrality is regulated by the (positive) ions and (negative) grains, while the peak of the charge distribution  $N_Z$  moves toward  $Z = 0$ . The magnitude of the average charge becomes comparable to the width of  $N_Z$  when  $\Psi \sim \sqrt{\tilde{\varphi}} (\ll 1)$ , which indicates a crossover to a DD plasma, occurring at the *asymptotic threshold*  $n_g \sim n_g^{\text{asy}}$ , Equation (21): Asymptotically, the charge neutrality is regulated by positively and negatively charged grains, the normalized ion density slightly increases and tends to  $1 + \Psi_{\text{EI}}$ , the normalized electron density approaches a small value of  $e^{-\Psi_{\text{EI}}}$ , while  $\Psi$  tends to zero as  $\propto (n_g/\zeta)^{-1}$ . The behavior at  $n_g \gtrsim n_g^{\text{dep}}$  can be also described by approximate relations, Equations (18)–(20), depicted by the red dashed lines. Note that in a DD plasma, the electrostatic repulsion between charged grains virtually disappears and a “coagulation window” opens up (allowing a growth of large aggregates, as discussed in Section 6.1).

where small terms  $1/(\sqrt{\tilde{m}}\tilde{\varphi})$  were neglected. The governing Equations (11) and (12) are reduced to

$$\zeta n_g = 2\sqrt{2\pi} v_i n_i (1 + \sqrt{\tilde{m}}) a^2 N_0, \quad (24)$$

$$n_i - n_e = (1 - \tilde{m}^{-1}) N_{-1}, \quad (25)$$

where  $\tilde{m} = (n_e/n_i)^2 \tilde{m}_{\text{EI}}$ . By substituting Equation (23) in Equation (25) we obtain the average charge

$$|\langle Z \rangle| = \frac{1 - \tilde{m}^{-1}}{1 + \tilde{\varphi}/\sqrt{\tilde{m}}}, \quad (26)$$

which is always smaller than unity and, as expected, tends to zero when  $\tilde{m} \rightarrow 1$ .

For an EI plasma one should set  $\tilde{m} = \tilde{m}_{\text{EI}}$  and neglect the rhs of the charge-neutrality Equation (25), exactly as in the case  $\tilde{\varphi} \ll 1$ . The corresponding electron depletion

threshold is determined by

$$\left(\frac{n_g}{\zeta}\right)_{\text{dep}} = \frac{(m_d/m_g)^2 (1 + \tilde{\varphi}/\sqrt{\tilde{m}_{\text{EI}}})^2}{4\sqrt{2\pi} f_d^2 v_i a^2 \tilde{\varphi}}, \quad (27)$$

and the plasma density for  $n_g \lesssim n_g^{\text{dep}}$  is

$$\frac{n_{\text{EI}}}{\zeta} = 2f_d \frac{m_g}{m_d} (1 + \tilde{\varphi}/\sqrt{\tilde{m}_{\text{EI}}})^{-1} \left(\frac{n_g}{\zeta}\right)_{\text{dep}}. \quad (28)$$

We take into account that  $\tilde{m}_{\text{EI}}$  is very large, so the terms  $\sim \tilde{m}_{\text{EI}}^{-1}$  and  $\sim 1/\sqrt{\tilde{m}_{\text{EI}}}$  are omitted in both expressions (whereas the retained terms  $\tilde{\varphi}/\sqrt{\tilde{m}_{\text{EI}}}$  may be arbitrary large in the considered case).

For a DI plasma,  $n_g \gtrsim n_g^{\text{dep}}$ , we derive the following

relations:

$$(1 - \tilde{m}^{-1})(1 + 1/\sqrt{\tilde{m}}) \left( \frac{1 + \tilde{\varphi}/\sqrt{\tilde{m}_{\text{EI}}}}{1 + \tilde{\varphi}/\sqrt{\tilde{m}}} \right)^2 \simeq \frac{(n_g/\zeta)_{\text{dep}}}{(n_g/\zeta)}, \quad (29)$$

$$\frac{n_i}{n_{\text{EI}}} \simeq (1 + 1/\sqrt{\tilde{m}})^{-1} \left( \frac{1 + \tilde{\varphi}/\sqrt{\tilde{m}}}{1 + \tilde{\varphi}/\sqrt{\tilde{m}_{\text{EI}}}} \right). \quad (30)$$

Equation (29) yields the solution for  $\tilde{m}(n_g)$  and, hence, for  $n_e/n_i = \sqrt{\tilde{m}/\tilde{m}_{\text{EI}}}$ ; the dependence  $n_i(n_g)$  is obtained by substituting  $\tilde{m}(n_g)$  in Equation (30). Asymptotically we obtain  $\tilde{m} - 1 \propto |\langle Z \rangle| \propto \zeta/n_g$  and  $n_i \propto \zeta$ .

Thus, the qualitative behavior of  $n_e$ ,  $n_i$ , and  $|\langle Z \rangle|$  remains exactly the same as in the case  $\tilde{\varphi} \ll 1$ . On the other hand, the values of  $n_g^{\text{dep}}$  (Equations (16) or (27)) and  $n_{\text{EI}}$  (Equations (17) or (28)) can be quite different in the two cases – their relative magnitudes depend on  $\Psi_{\text{EI}}$  and  $\tilde{\varphi}$  (for the corresponding case). Nevertheless, the curves for the normalized electron and ion densities, plotted versus the normalized gas density in the case  $\tilde{\varphi} \gg 1$ , look similar to those in Figure 2. Interestingly, the absolute value of the asymptotic ion density  $n_i(n_g)$  for  $\tilde{\varphi} \gg 1$  is exactly a half of that derived for  $\tilde{\varphi} \ll 1$ . The dust charge distribution gradually changes at  $n_g \gtrsim n_g^{\text{dep}}$ , from the asymmetric triplet with the maximum at  $Z = -1$ , as given by Equation (9) with  $\tilde{m} = \tilde{m}_{\text{EI}}$ , to a quasi-symmetric triplet  $N_{\pm 1}/N_0 \simeq \tilde{\varphi}^{-1}$  with the peak at  $Z = 0$ . This latter asymptotic form represents a DD plasma discussed in Section 4.1.

Above, we have completely neglected the polarization interactions of electrons and ions with dust grains. These interactions noticeably increase the electron/ion collection cross sections by uncharged (or weakly charged) grains in the case  $\tilde{\varphi} \gg 1$  (Draine & Sutin 1987). As a result, the relative abundances  $N_{\pm 1}/N_0$  in Equation (9) are increased by the factor of  $\simeq \sqrt{\pi\tilde{\varphi}/8}$ . Correspondingly,  $\sqrt{\tilde{m}}$  in Equations (22) and (23) should be multiplied with this factor, while  $\sqrt{\tilde{m}}$  in Equation (24) should be multiplied with  $\sqrt{\pi\tilde{\varphi}/2}$ , and Equation (25) is left unchanged. In practice, such modification does not affect the characteristic densities given by Equations (27) and (28), as it becomes important only for extremely large values of  $\tilde{\varphi} \gtrsim \tilde{m}$  ( $\sim 5 \times 10^4$  for a  $\text{HCO}^+/\text{N}_2\text{H}^+$  plasma).

To conclude this Section, let us make a note on a crossover between the limiting cases  $\tilde{\varphi} \ll 1$  and  $\tilde{\varphi} \gg 1$ . In an EI plasma, the magnitude of the average charge given by Equation (26) is always significantly smaller than  $|\langle Z_{\text{EI}} \rangle| (= \Psi_{\text{EI}}/\tilde{\varphi})$  for  $\tilde{\varphi} \ll 1$ . This fact does not allow us to smoothly match these two cases: From Equations (16) and (27) we conclude that the value of  $(n_g/\zeta)_{\text{dep}}$  for  $\tilde{\varphi} \gg 1$  is a factor of  $\Psi_{\text{EI}}(1 + \Psi_{\text{EI}})$  larger than that for  $\tilde{\varphi} \ll 1$ , when compared at the formal “matching point”  $\tilde{\varphi} = 1$ . Similarly, from Equations (17) and (28) we obtain that  $n_{\text{EI}}/\zeta$  calculated at the matching point for  $\tilde{\varphi} \gg 1$  is  $1 + \Psi_{\text{EI}}$  times the value for  $\tilde{\varphi} \ll 1$ . Setting for simplicity  $\zeta = \text{const}$  and taking a  $\text{HCO}^+/\text{N}_2\text{H}^+$  plasma as an example, we obtain the relative mismatch of  $\simeq 19$  for  $n_g^{\text{dep}}$  and  $\simeq 4.8$  for  $n_{\text{EI}}$ . The reason for the discrepancy is obvious: Equations (B1) and (B2) imply that

the negatively charged states with  $|Z| \geq 2$ , neglected in Equations (24) and (25), rapidly become dominant when  $\tilde{\varphi}$  decreases below a value of  $\simeq \ln \sqrt{\tilde{m}_{\text{EI}}} (\simeq 5.4$  for a  $\text{HCO}^+/\text{N}_2\text{H}^+$  plasma). Hence, there is a relatively narrow range ( $1 \lesssim \tilde{\varphi} \lesssim \ln \sqrt{\tilde{m}_{\text{EI}}}$ ) where the states with  $|Z| \geq 2$  must be taken into account.

## 5. EFFECT OF GRAIN-SIZE DISTRIBUTION

The grain polydispersity, i.e., the presence of grains of different sizes, plays an exceptionally important role in the discussed processes. The reason for that is twofold, as one can directly see from the governing equations: The integral in the ionization-recombination Equation (11) determines the magnitude of the plasma recombination rate on the grain surface and, hence, the equilibrium plasma (ion) density. The integral can be dominated by different parts of the size distribution, depending on its particular form. In the same way, the size distribution affects the integral determining the contribution of charged grains in the charge-neutrality Equation (12).

Let us first consider the case  $\tilde{\varphi} \ll 1$  which, remarkably, allows us to obtain rigorous results for arbitrary size distribution from the solution derived in Section 4.1 for single-size grains. Indeed, keeping the integrals in Equations (11) and (12) yields in this case Equations (14) and (15) with the modified rhs: The factor  $a^2 n_d$  in the former equation is replaced with  $\int dn_d a^2$ , and, similarly,  $\tilde{\varphi}^{-1} n_d$  in the latter equation is replaced with  $\int dn_d \tilde{\varphi}^{-1}$  (we remind that  $\tilde{\varphi}^{-1} \propto a$ ). Thus, the effects of polydispersity are *factorized*, leading to a simple renormalization of the characteristic densities.

For illustration, we employ a widely used power-law dependence for the differential dust density,

$$dn_d(a)/da = Ca^{-p}, \quad (31)$$

defined for the size range  $a_{\min} \leq a \leq a_{\max}$  (we naturally assume that the condition  $\tilde{\varphi} \ll 1$  is satisfied for all sizes down to  $a_{\min}$ ). The constant  $C$  is determined from the dust-to-gas density ratio, Equation (2), where the product  $m_d n_d$  should be replaced by the integral  $\int dn_d m_d$ . For certainty, we assume that the power-law index  $p$  does not exceed the MRN value of 3.5 (Kim et al. 1994; Weingartner & Draine 2001), so the mass integral is always dominated by the upper-size cutoff  $a_{\max}$ . For this size distribution, the integral  $\int dn_d a^2$  in the modified Equations (14) is equal to  $a_{\max}^2 n_d$  multiplied by the following renormalization factor:

$$\frac{4-p}{|3-p|} \begin{cases} 1, & p < 3; \\ \tilde{a}^{p-3}, & p > 3. \end{cases} \quad (32)$$

Here,  $\tilde{a} \equiv a_{\max}/a_{\min} \gg 1$  and  $n_d$  is the effective dust density determined by the condition  $\int dn_d m_d = m_{d,\max} n_d$ , with  $m_{d,\max} \equiv m_d(a_{\max})$ . For the sake of clarity we do not consider situations with  $p \simeq 3$  (where the contributions of the upper and lower cutoffs are comparable), which allows us to neglect small terms  $\propto \tilde{a}^{-|p-3|}$ . Similarly, the integral  $\tilde{\varphi}^{-1} n_d$  in the modified Equation (15) is equal to  $\tilde{\varphi}_{\max}^{-1} n_d$  multiplied by the renormalization factor

$$\frac{4-p}{|2-p|} \begin{cases} 1, & p < 2; \\ \tilde{a}^{p-2}, & p > 2, \end{cases} \quad (33)$$



where  $\tilde{\varphi}_{\max} \equiv \tilde{\varphi}(a_{\max})$ . We see that the contribution of smaller grains can become dominant when  $dn_d(a)/da$  decreases sufficiently steeply with size. This lowers the plasma density (due to enhanced recombination) and increases the average grain charge, as described by Equations (32) and (33), respectively.

From Equations (32) and (33) we infer that the characteristic densities can be dramatically decreased for polydisperse grains: From Equation (3) we conclude that the resulting recombination threshold  $(n_g/\zeta)_{\text{rec}}$  is inversely proportional to the squared recombination rate and, hence, is reduced by the *squared* factor (32). For the MRN distribution this implies a decrease by a factor of about  $a_{\max}/a_{\min} \simeq 50$  (Mathis et al. 1977). As for the electron depletion threshold  $(n_g/\zeta)_{\text{dep}}$ , its value is inversely proportional to the product of the two factors, i.e., the rhs of Equation (16) should be divided by

$$\frac{(4-p)^2}{|(2-p)(3-p)|} \begin{cases} 1, & p < 2; \\ \tilde{a}^{p-2}, & 2 < p < 3; \\ \tilde{a}^{2p-5}, & p > 3. \end{cases} \quad (34)$$

Again, taking the MRN distribution as an extreme example, we obtain a reduction by almost three orders of magnitude! Finally, the density of an EI plasma, Equation (17), is directly derived from Equation (14) and hence is unaffected by the charge density associated with grains. Therefore,  $n_{\text{EI}}/\zeta$  for polydisperse grains should only be reduced by the factor (32).

In the case  $\tilde{\varphi} \gg 1$ , the effects of polydispersity are generally no longer factorized: Now, the factors  $a^2 N_0$  and  $N_{-1}$  on the rhs of Equations (24) and (25), respectively, should be replaced with integrals. Using Equations (22) and (23) we obtain the respective integrals,  $\int dn_d a^2 (1 + \sqrt{\tilde{m}}/\tilde{\varphi})^{-1}$  and  $\int dn_d (1 + \tilde{\varphi}/\sqrt{\tilde{m}})^{-1}$ . One can see that a renormalization of the characteristic densities is only possible when the range of  $\tilde{\varphi}$  (corresponding to a given range of grain sizes) does not overlap with the value of  $\sqrt{\tilde{m}}$ . As the latter decreases monotonically with  $n_g$ , from  $\sqrt{\tilde{m}_{\text{EI}}} (= 231 \text{ for a } \text{HCO}^+/\text{N}_2\text{H}^+ \text{ plasma})$  to unity, such situation appears unlikely, and thus the governing equations should be solved numerically. Nevertheless, in the following Section (where the numerical results are presented) we demonstrate that the qualitative effect of polydispersity remains similar to that discussed above for the case  $\tilde{\varphi} \ll 1$ .

## 6. IMPLICATIONS FOR PROTOPLANETARY DISKS

In this Section we employ a typical protoplanetary disk model to numerically calculate the gas ionization and dust charging. The results are aimed to answer the following questions:

- May the “coagulation window” be opened, to overcome the electrostatic barrier?
- How accurate is the (conventional) assumption of low dust charges?
- Should the ionization and dust evolution models be mutually consistent?

We restrict ourselves by considering the disk midplane region, where the gas and dust mass is concentrated. The gas surface density of the disk is assumed to obey

a power-law dependence on the disk radius,  $\Sigma(R) = \Sigma_{\text{AU}}(R/\text{AU})^{-q}$  with  $\Sigma_{\text{AU}} = 200 \text{ g/cm}^2$  and  $q = 1$ , which leads to the disk mass of  $0.02 M_{\odot}$  ( $0.04 M_{\odot}$ ) for the outer radius of 150 AU (300 AU). We consider a sharp cutoff, as a tapered power-law profile does not qualitatively change the results. Furthermore, we assume that the disk thermal structure is determined by re-radiation of the central star emission. The gas/dust temperature is calculated from  $T^4(R) = T_*^4(R_*/R)^2 \sin \phi$  (Brauer et al. 2008) with the effective star temperature  $T_* = 4000 \text{ K}$ , stellar radius  $R_* = 2.6 R_{\odot}$ , and  $\sin \phi = 0.05$  for the sine of the grazing angle.<sup>6</sup> The disk is assumed to be vertically isothermal, with the vertical density structure derived from the hydrostatic equilibrium for the central star mass of  $M_* = 0.7 M_{\odot}$ . We consider CRs, stellar X-rays and radionuclides as primary sources of ionization in the midplane (Turner & Sano 2008),

$$\zeta(R) = \zeta_{\text{CR}} e^{-\frac{\Sigma(R)}{2\Sigma_{\text{CR}}}} + \frac{\zeta_{\text{XR}}}{(R/\text{AU})^2} e^{-\frac{\Sigma(R)}{2\Sigma_{\text{XR}}}} + \zeta_{\text{RA}}, \quad (35)$$

where  $\zeta_{\text{CR}} = 10^{-17} \text{ s}^{-1}$  is the (unattenuated) CR-ionization rate with the attenuation surface density of  $\Sigma_{\text{CR}} = 96 \text{ g/cm}^2$ ,  $\zeta_{\text{XR}} = 5.2 \times 10^{-15} \text{ s}^{-1}$  is the X-ray ionization rate at 1 AU (which corresponds to the X-ray luminosity of the central star of  $\simeq 2 \times 10^{30} \text{ erg/s}$ ) with the attenuation surface density of  $\Sigma_{\text{XR}} = 8 \text{ g/cm}^2$ , and  $\zeta_{\text{RA}} = 10^{-21} \text{ s}^{-1}$  is the ionization rate due to long-lived radioactive nuclei.

An important ingredient of any disk model are dust properties, i.e., the dust density, size distribution, and grain morphology. Below we consider four characteristic models for the dust size distribution – two “monodisperse” (single-size) populations of grains, and two MRN-like distributions (Mathis et al. 1977), given by Equation (31) with  $p = 3.5$ :

- monodisperse,  $a = 0.1 \mu\text{m}$ ;
- monodisperse,  $a = 10 \mu\text{m}$ ;
- MRN:  $a_{\min} = 0.005 \mu\text{m}$ ,  $a_{\max} = 0.25 \mu\text{m}$ ;
- evolved MRN:  $a_{\min} = 0.5 \mu\text{m}$ ,  $a_{\max} = 25 \mu\text{m}$ .

For all models, grains are supposed to be compact spheres, and the dust-to-gas ratio is the same and equal to  $f_d = 0.01$  at any location in the disk. We adopt  $3.5 \text{ g/cm}^3$  for the solid mass density of dust grains, and assume that  $\text{N}_2\text{H}^+$  or  $\text{HCO}^+$  are the dominant ions ( $A = 29$ ).

### 6.1. May the “coagulation window” be opened?

The electrostatic barrier against the dust growth, caused by the mutual repulsion of the negatively charged grains (Okuzumi 2009), presents a fundamental but still poorly investigated issue of the modern dust evolution models. The issue stems from estimates (Okuzumi 2009) showing that in most regions of a protoplanetary disk the average electrostatic energy of the grain-grain interaction

<sup>6</sup> The additional gas heating due to accretion may increase the inner disk temperature, leading to thermal ionization. Here we neglect this effect, since it is only important at high temperatures above  $\sim 1000 \text{ K}$ .

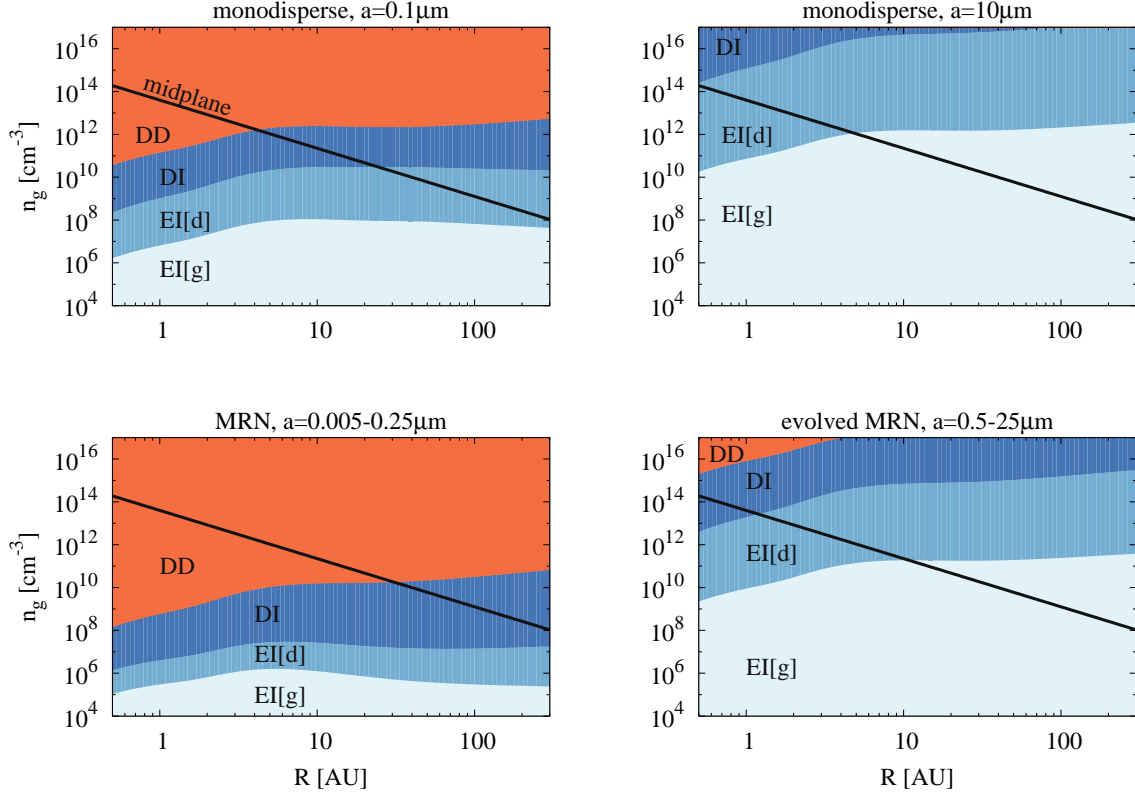


FIG. 3.— Gas number density  $n_g$  in the disk midplane versus the radial distance  $R$  (black solid line), plotted for the assumed disk model. Different panels represent different models for the dust size distribution (as indicated, see text for details). Boundaries between different regions in each panel are the thresholds  $(n_g/\zeta)_{\text{rec}}$ ,  $(n_g/\zeta)_{\text{dep}}$ , and  $(n_g/\zeta)_{\text{asy}}$  plotted as functions of  $R$  and separating, respectively, electron-ion plasmas with the gas-phase (EI[g]) and dust-phase (EI[d]) recombination, dust-ion plasmas (DI), and dust-dust plasmas (DD).

typically exceeds their relative kinetic energy. The two obvious ways to overcome the barrier are to decrease the magnitude of the grain charges or to increase the relative velocity of the grains. Recently it was shown that the photoelectric emission caused by stellar UV radiation may drive grain charges to positive values and thus allow dust coagulation at intermediate heights of the protoplanetary disks (Akimkin 2015); similarly, the photoelectric grain charging due to CR-induced  $\text{H}_2$  fluorescence can operate in the much deeper, outer midplane regions of the disk (Ivlev et al. 2015). None of these mechanisms, however, is able to affect dust charging in dense disk regions. Okuzumi et al. (2011a) suggested that the presence of a large number of small grains may remove free electrons from the gas in these regions, and thus make larger grains less charged. Let us elaborate on the latter mechanism.

Under low-density/high-ionization conditions with  $n_g/\zeta \lesssim (n_g/\zeta)_{\text{dep}}$  (EI plasmas), grains are highly charged due to abundance of free electrons. The average grain charge in this case tends to the maximum possible value of  $\tilde{\varphi}^{-1}\Psi_{\text{EI}}$ , determined by the ion mass and temperature, and therefore the coagulation of micron-size (or larger) grains is usually hampered. In denser regions of the disk, where  $(n_g/\zeta)_{\text{dep}} < n_g/\zeta < (n_g/\zeta)_{\text{asy}}$  (DI plasmas), the grain charges lower due to depletion of free electrons. A specific feature of DI plasmas is that charging of grains of a given size is determined by the entire dust ensemble. By moving into the densest disk regions, where  $n_g/\zeta > (n_g/\zeta)_{\text{asy}}$  (DD plasmas), the depletion of

electrons eventually becomes so strong that their accretion onto a neutral grain is practically equal to the ion accretion. Thus, the grain charge distribution becomes practically symmetric with respect to zero, opening up the opportunity for barrier-free coagulation.

The threshold parameters  $(n_g/\zeta)_{\text{rec}}$ ,  $(n_g/\zeta)_{\text{dep}}$ , and  $(n_g/\zeta)_{\text{asy}}$ , identifying boundaries between different plasma regions, vary across the disk. As introduced above,  $(n_g/\zeta)_{\text{rec}}$  is determined by equal gas and dust contributions to the recombination rates,  $(n_g/\zeta)_{\text{dep}}$  corresponds to equal number densities of free electrons and electrons carried by dust grains, while at  $(n_g/\zeta)_{\text{asy}}$  the total positive charge is equally distributed between free ions and grains. We express these parameters in terms of the gas density, with the ionization rate according to Equation (35), and depict the resulting plasma regions EI[g], EI[d], DI, and DD in Figure 3 for the four dust models.

Figure 3 shows that for the monodisperse  $0.1 \mu\text{m}$  dust model (upper left panel), the DD plasma region is limited to  $R \lesssim 4 \text{ AU}$  and the EI region is at  $R \gtrsim 20 \text{ AU}$  (with the DI region filling the gap between them). Introducing the grain polydispersity leads to a strong shift of the plasma boundaries: for the MRN model (lower left panel), the DD plasma region extends up to  $R \sim 30 \text{ AU}$ , while the DI region continues beyond  $R \sim 300 \text{ AU}$ . These results confirm conclusions of Section 5, demonstrating that excess of small particles in a broad size distribution may dramatically reduce the values of  $(n_g/\zeta)_{\text{dep}}$  and  $(n_g/\zeta)_{\text{asy}}$ . The increase of the overall grain size has the

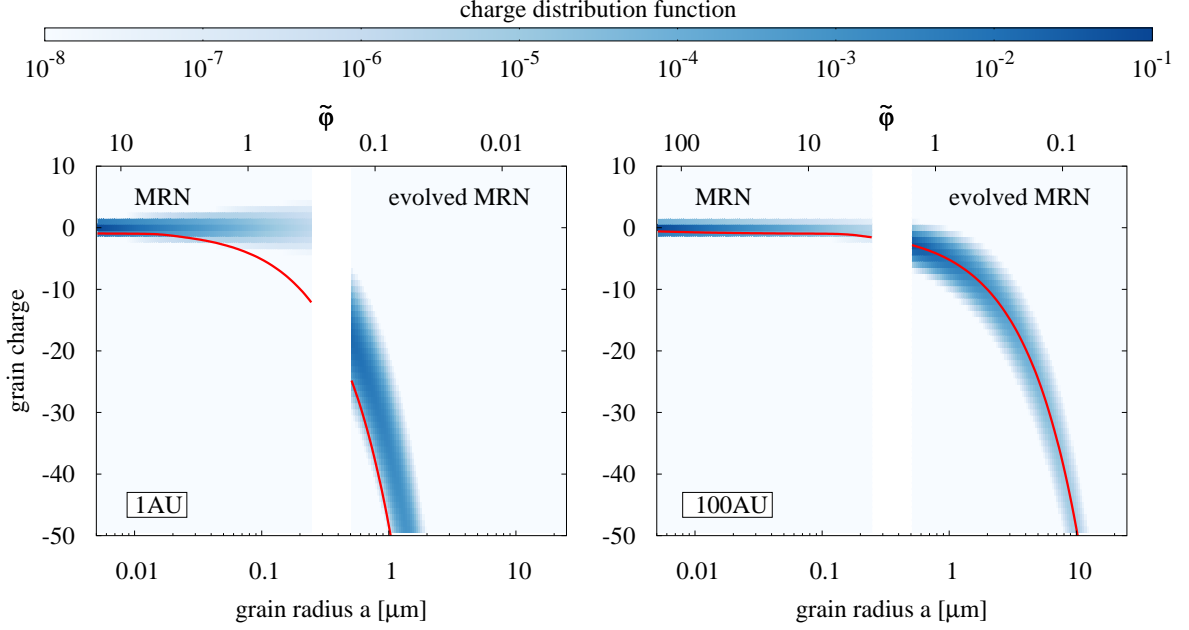


FIG. 4.— Grain charge distribution  $N(Z, a)$  for different regions in the disk midplane. The results are for two characteristic dust size distributions: MRN [ $0.005 \mu\text{m}$ ,  $0.25 \mu\text{m}$ ] and evolved MRN [ $0.5 \mu\text{m}$ ,  $25 \mu\text{m}$ ], the upper horizontal axis shows the corresponding values of  $\tilde{\varphi}$ . The blue scale denotes the relative number density of charged grains ( $N_Z$  normalized by the total dust density  $n_d$ ) at the radial distance of  $R = 1$  AU (left) and  $100$  AU (right); the respective physical conditions are  $T = 208$  K,  $n_g = 4 \times 10^{13} \text{ cm}^{-3}$ ,  $\zeta = 4 \times 10^{-18} \text{ s}^{-1}$  (left) and  $T = 21$  K,  $n_g = 10^9 \text{ cm}^{-3}$ ,  $\zeta = 10^{-17} \text{ s}^{-1}$  (right). The red solid line shows the mean grain charge calculated neglecting the charge depletion effects (i.e., assuming  $n_e = n_i$ ).

opposite effect: According to the results of Sections 4.1 and 4.2, the boundaries between different plasma regions in this case are shifted to much higher  $n_g$  (i.e., to smaller  $R$ ), with the strongest effect being on  $(n_g/\zeta)_{\text{dep}} \propto a^4$  (for monodisperse grains). Indeed, the right panels in Figure 3, depicting the results for monodisperse  $10 \mu\text{m}$  grains and for the evolved MRN model, show no presence of a DD plasma.

Thus, the (initial) MRN size distribution ensures that the coagulation window is opened (DD plasma state) in the entire inner disk, promoting rapid dust growth. However, the latter process rapidly modifies the overall charge balance towards DI and EI plasmas: for the evolved dust distributions (only by two orders of magnitude in size, as in the right panels of Figure 3) the electrostatic barrier is completely restored (EI plasma state) for  $R \gtrsim 1$  AU. The excess of small grains makes the coagulation conditions more favorable, but this factor alone is insufficient for further efficient dust growth.

We conclude that some feedbacks are necessary to facilitate the coagulation. This could be dust fragmentation leading to, e.g., a bimodal small/big size distribution (where small grains provide conditions for a reduced potential barrier between big grains, Okuzumi et al. 2011a); or this could be an increase in the dust-to-gas ratio  $f_d$  (Booth & Clarke 2016; Surville et al. 2016), since both the EI-DI and DI-DD plasma boundaries are determined by the value of  $(n_g/\zeta)_{\text{dep}} \propto f_d^{-2}$ . Such feedbacks may be achieved by setting up a turbulent motion which, simultaneously, increases the relative grain velocities (Testi et al. 2014) and hence further reduces the effect of the electrostatic barrier. Turbulence generates local dust traps (van der Marel et al. 2013) where  $f_d$  can become as high as a few (Johansen & Youdin 2007;

Surville et al. 2016). With such values of  $f_d$ , the coagulation window opens up at  $R \sim 1$  AU even for the monodisperse  $10 \mu\text{m}$  dust (while for the evolved MRN,  $f_d \simeq 0.2$  is sufficient).

#### 6.2. Low charges for dust grains: Is this always justified?

In the contemporary MRI and astrochemical models of protoplanetary disks, it is routinely assumed that the charge states of dust grains are around zero ( $0, \pm 1, \pm 2$ ). This is generally true for small dust grains ( $a \lesssim 0.1 \mu\text{m}$ ) in low-temperature gas ( $T \lesssim 100$  K) (Tielens 2005, see Equation (5.75)). However, such small grains cannot be representative for the dense protoplanetary environments. As the average charge of larger grains scales linearly with the size, the coagulation inevitably leads to the breakdown of the low-charge assumption (see also Perez-Becker & Chiang 2011; Ilgner 2012).

In Figure 4 we demonstrate the grain charge distributions for the MRN and evolved MRN models, plotted at the radial distance of  $1$  AU (left) and  $100$  AU (right). Note that different dust models correspond to independent simulations and are only shown on the same plot to facilitate the comparison.

In the MRN case shown in Figure 4 most grains, indeed, carry low charges. For  $R = 1$  AU, the charge distribution is practically symmetric with respect to the zero state. This symmetry is a characteristic feature of DD plasmas, where the singly-charged positive and negative grains are the dominant charge carriers. For  $R = 100$  AU, the charge distribution is slightly shifted to the negative values, representing DI plasmas. Low grain charges in the MRN case are due to a large number of small ( $a \lesssim 0.01 \mu\text{m}$ ) grains – they effectively reduce the abundance of free electrons and prevent larger (sub-

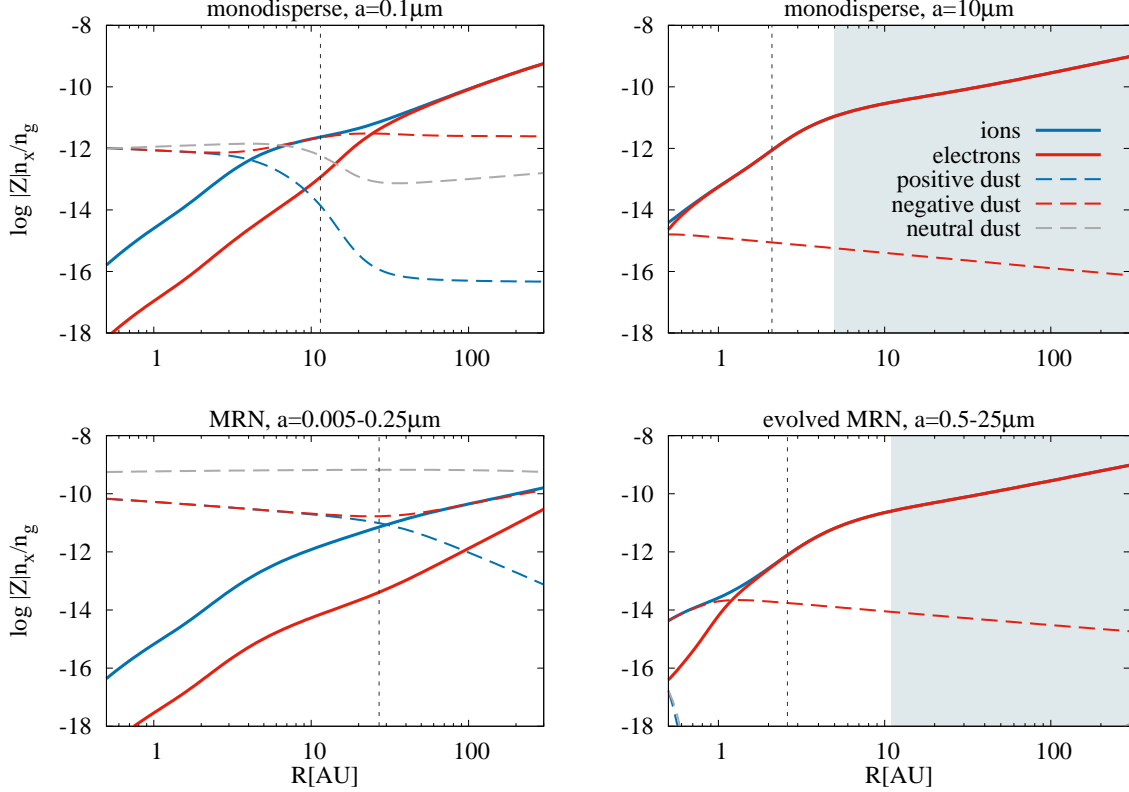


FIG. 5.— Relative “charge abundance” of different species in the disk midplane,  $|Z|n_x/n_g$ , versus the radial distance  $R$ . The abundances, plotted for different models of the dust size distribution (as indicated), are defined as  $n_{i,e}/n_g$  for ions and electrons,  $\sum_{Z>0} \int da ZN_Z/n_g$  for positive dust,  $\sum_{Z<0} \int da |Z|N_Z/n_g$  for negative dust, and  $\int da N_0/n_g$  for neutral dust. The vertical dashed line in each panel indicates the outer boundary of the dead zone. The shaded regions show EI[g] plasmas where the results become inaccurate.

micron) grains from being multiply charged. However, as small grains are expected to disappear rapidly during the initial stages of coagulations, larger grains become dominant in the size distribution.

For the evolved MRN distribution in Figure 4, the average grain charge exhibits a linear scaling with the size; the charge may be as high as  $-50$  for  $1 \mu\text{m}$  grains. We notice that the results for  $R = 1$  AU and  $100$  AU represent, respectively, DI plasmas and EI plasmas (as follows from the lower right panel of Figure 3), so their direct comparison may appear counterintuitive: for otherwise the same parameters, dust charges in DI plasmas should be lower than in EI plasmas. The observed “discrepancy” is, however, due to the fact that temperatures are higher at smaller  $R$ .

The derived charge distributions show that one should be careful assuming low-charge states for protoplanetary disk conditions. A moderate increase of the average grain size (above  $\sim 1 \mu\text{m}$ ) can easily break this assumption.

### 6.3. Models of ionization and dust evolution: Should they be mutually consistent?

The “dead zone” is a region of the protoplanetary disk where the development of MRI is suppressed by non-ideal MHD effects (e.g., Armitage 2007). It is well known that the size of the dead zone should strongly depend on dust properties (Sano et al. 2000; Bai 2011a,b; Dudorov & Khaibrakhmanov 2014). The inner boundary of the dead zone is associated with the thermal ionization near the central star, and is usually located at

distances well below  $1$  AU (Chatterjee & Tan 2014). To estimate the position of the outer boundary, we use the condition that the magnetic Reynolds number,

$$\text{Re}_{\text{mag}} = \frac{\alpha^{1/2} c_s^2}{\eta_0 \Omega_K}, \quad (36)$$

exceeds unity outside of the dead zone (see, e.g., Equation (170) of Armitage 2015). Here,  $\alpha \sim 10^{-3}$  is the turbulent alpha-parameter (outside of the dead zone),  $c_s = \sqrt{k_B T / (2.3 m_p)}$  is the sound speed, and  $\Omega_K = \sqrt{GM_*/R^3}$  is the Keplerian angular velocity. For the estimates, we assume that the magnetic diffusivity  $\eta$  at high gas densities is dominated by the Ohmic term (Xu & Bai 2016), which can be approximated by  $\eta_0 = 234 (n_g/n_e) \sqrt{T/K}$  for a weakly ionized gas (Spitzer 1962; Armitage 2011). It is noteworthy that the Hall and ambipolar diffusivities also contribute to non-ideal MHD effects (e.g., Bai 2011a; Zhao et al. 2016); in particular, a preponderance of submicron dust in the size distribution makes the ambipolar contribution dominant even at high  $n_g$ . However, all these terms become relatively small as the size distribution evolves toward larger grains (Zhao et al. 2016).

To demonstrate the influence of the grain size distribution on the size of the dead zone, in Figure 5 we plot the abundances of the major charged species, calculated for different dust models. One can see that even a moderate increase in the average grain size leads to significant changes in the ionization degree which, in turn, strongly



affects the position of the outer dead-zone boundary, marked by the vertical dashed line in each panel: The resulting size of the dead zone is approximately 27, 11, 2.6 and 2.1 AU for, respectively, the MRN, monodisperse  $0.1 \mu\text{m}$ , evolved MRN, and monodisperse  $10 \mu\text{m}$  dust size distribution.

As was pointed out in Section 6.1, dust coagulation increases the ionization degree which, in turn, leads to higher grain charges and prevents further coagulation due to growing electrostatic barrier. On the other hand, higher ionization favors the development of MRI and thus stimulates the coagulation via turbulent dust motion. The situation become even more complicated when the turbulence leads to the fragmentation of dust aggregates – apart from destruction, this process generates new populations of small dust which may reduce the electrostatic barrier and promote the further coagulation of larger grains. Altogether, this suggests the existence of “positive” and “negative” feedback loops that may unpredictably halt or accelerate the coagulation at different locations in the disk, and also highlights the importance of self-consistent analysis of the ionization and dust evolution processes.

## 7. SUMMARY

It is well-known that the ionization fraction is a crucial parameter for the dynamical evolution of star forming regions (e.g., McKee 1989). Recently, it has also been shown that the formation of protoplanetary disks strongly depends on the grain size distribution and ionization structure of a contracting dense cloud core (Zhao et al. 2016). In the present paper, we have developed an exact analytical model which describes the behavior of the charged species (electrons, ions, and dust) and provides the dust charge distribution for dense protoplanetary disk conditions, for arbitrary grain size distribution (the governing equations for different cases are summarized in Appendix A, Table 2).

The model has only one free parameter, the effective mass of the ions  $A$ , and is developed for the conditions where the dust-phase recombination of free electrons and ions dominates over the gas-phase recombination. A transition to this regime occurs in an electron-ion (EI) plasma (where charged grains still do not play any role in the overall charge neutrality), and is characterized by the dust-phase recombination threshold  $(n_g/\zeta)_{\text{rec}}$  for the gas density.

At higher gas densities,  $n_g/\zeta \gtrsim (n_g/\zeta)_{\text{rec}}$ , charged grains play an increasingly important role in the charge neutrality. We have determined two characteristic parameters, the electron depletion threshold  $(n_g/\zeta)_{\text{dep}} \gg (n_g/\zeta)_{\text{rec}}$  and the asymptotic threshold  $(n_g/\zeta)_{\text{asy}} \gg (n_g/\zeta)_{\text{dep}}$ , marking, respectively, transitions from the EI to dust-ion (DI) plasma state, and then to the dust-dust (DD) state. The thresholds are determined in such a way that at  $n_g/\zeta = (n_g/\zeta)_{\text{dep}}$  electrons and negative grains equally contribute to the total negative charge, while at  $n_g/\zeta = (n_g/\zeta)_{\text{asy}}$  ions and positive grains provide equal contribution to the total positive charge.

The presented model allowed us to identify universality in the behavior of charged species at high gas densities. Let us summarize important implications of the derived results for protoplanetary disks:

1. Unless the dust size distribution is dominated by grains much smaller than  $\sim 1 \mu\text{m}$ , larger grains are typically multiply (negatively) charged. In this case, irrespective of the location in the disk, the average grain charge scales linearly with the size. As the size distribution in protoplanetary disk conditions develops towards bigger grains, the conventional approximation of low grain charges may only be used for (very) initial stages of the disk evolution.
2. The asymptotic transition to a DD plasma implies that the grain charge distribution becomes quasi-symmetric with respect to  $Z = 0$ . This completely removes the repulsive electrostatic barrier and opens a “coagulation window” for large aggregates, operating in the inner dense region of protoplanetary disks. On the other hand, the coagulation itself leads to decreasing dust number density and a gradual shift back to the DI/EI plasma states. The (re)appearance of the electrostatic barrier in this case (with the maximum achieved in the EI state) may completely inhibit further dust growth. The barrier can be reduced by various feedback mechanisms operating in the disk and leading to increased local gas-to-dust ratio, such as the dust trapping or moderate fragmentation.
3. The dust evolution, change in the charged species abundances, and development of the magnetorotational instability (MRI) are strongly interrelated processes whose mutual effect is poorly understood: The dust coagulation increases the ionization degree which, in turn, leads to higher grain charges and prevents further coagulation due to growing electrostatic barrier. On the other hand, higher ionization favors the development of MRI, making a disk turbulent; a moderate turbulence facilitates dust growth by increasing the relative grain velocities, while strong turbulence leads to dust fragmentation. The latter generates small grains, which may decrease the electron fraction (asymptotically, by a factor of  $\sqrt{m_i/m_e} \sim 10^2$ ) and lead to MRI quenching. A complex interplay of these nonlinear processes suggests the existence of multiple positive and negative feedback loops that may dramatically affect the ultimate dust evolution.

A rigorous treatment of the ionization fraction and dust evolution could be critical during all stages in the process that links molecular clouds to stellar systems – this is the motivation behind our work. The exact analytic model presented here can be easily implemented in non-ideal MHD simulations, to properly follow the ionization fraction and the dust growth during the process of protoplanetary disk formation (e.g., Zhao et al. 2016) and evolution (e.g., Dullemond et al. 2007; Armitage 2011, and references therein).

We provide a FORTRAN source code, applicable for arbitrary dust size distributions, for calculating abundances of the charged species: <http://www.inasan.ru/~akimkin/codes.html>

## ACKNOWLEDGEMENTS

This research made use of NASA’s Astrophysics Data System. The authors thank Dr. Bo Zhao for useful discussions. VVA acknowledges financial support from Russian Foundation for Basic Research (16-32-00012 mol.a)

and from a grant of the President of the Russian Federation (NSH-9576.2016.2). PC acknowledges financial support from the European Research Council (ERC Advanced Grant PALs 320620).

## APPENDIX

### APPENDIX A: SUMMARY OF GOVERNING EQUATIONS

For convenience, in Table 2 we list the equations to be used in a general case, as well as in different limiting cases.

TABLE 2

Dust size distribution; limiting case	Parameters	Governing equations	Auxiliary relations	Solution for
Polydisperse; arbitrary $\tilde{\varphi}$	$n_g, \zeta, f_d, T, A, dn_d/da$	(11)–(13), (B2), (B3)	(2), (4), (5), (6)	$n_i, n_e, N_Z$
Monodisperse; $\tilde{\varphi} \ll 1$	$n_g, \zeta, f_d, T, A, a$	(8), (14), (15)	(2), (5), (6), (7)	$n_i, n_e, \langle Z \rangle$
Monodisperse; $\tilde{\varphi} \gg 1$	$n_g, \zeta, f_d, T, A, a$	(22)–(24), (25)	(2), (5), (6), (9), (26)	$n_i, n_e, N_0, N_{-1}$

### APPENDIX B: GRAIN CHARGE DISTRIBUTION $N_Z$

When the photoemission from grains as well as other emission mechanisms are negligible,  $N_Z$  is determined by the collection of electrons and ions from the ambient plasma. The sticking probabilities of electrons and ions are both assumed equal to unity. The collection cross sections, determined by the electrostatic interactions with a charged grain, are derived from the so-called Orbital Motion Limited (OML) approximation (Whipple 1981; Fortov et al. 2005). For the positive-charge states, the detailed equilibrium yields (Draine & Sutin 1987; Draine 2011)

$$Z \geq 0: \quad \frac{N_{Z+1}}{N_Z} = \left( \frac{e^{-Z\tilde{\varphi}}}{1 + (Z+1)\tilde{\varphi}} \right) \frac{1}{\sqrt{\tilde{m}}}, \quad (\text{B1})$$

the negative-charge states are related to the respective positive states via

$$N_{-Z} = \tilde{m}^Z N_Z. \quad (\text{B2})$$

From Equation (B1) we derive

$$Z > 0: \quad \frac{N_Z}{N_0} = \frac{e^{-\frac{1}{2}Z(Z-1)\tilde{\varphi}}}{\tilde{m}^{Z/2} \prod_{Z'=1}^Z (1 + Z'\tilde{\varphi})}, \quad (\text{B3})$$

$N_{-Z}$  is readily obtained by using Equation (B2). Note that the charge distribution is slightly modified when the polarization interactions are taken into account (e.g., Equations (3.3) and (3.4) in Draine & Sutin 1987). If needed, this effect can easily be included in Equations (B1)–(B3) (Ivlev et al. 2015). To include the stickling probabilities of electrons,  $s_e(Z)$ , and ions,  $s_i(Z)$ , the rhs of Equation (B1) should be multiplied by the ratio  $s_i(Z)/s_e(Z+1)$ .

### APPENDIX C: EFFECTIVE DUST DENSITY $\mathcal{N}$ FOR THE ION COLLECTION

The effective number density  $\mathcal{N}(a)$  of grains of radius  $a$ , entering the dust-phase recombination term  $R_d$  in Equation (10), takes into account the electrostatic interaction between ions by charged grains. Depending on the sign of the grain charge, the (geometrical) cross section of the ion collection by the grain is increased or decreased; the corresponding factors are derived from the OML approximation. Summing up partial contributions of all charged states yields

$$\mathcal{N}(a) = \sum_{Z < 0} (1 - Z\tilde{\varphi}) N_Z + \sum_{Z \geq 0} e^{-Z\tilde{\varphi}} N_Z.$$

We use Equation (B2) to eliminate the summation over the positive-charge states, and employ the recurrent relation (B1) to rewrite  $\mathcal{N}$  in the identical form,

$$\mathcal{N}(a) = \sum_{Z \geq 0} (\sqrt{\tilde{m}} + \tilde{m}^{-Z}) e^{-Z\tilde{\varphi}} N_{-Z}, \quad (\text{C1})$$

which is more convenient for the analysis (see Sections 4.1 and 4.2).

## REFERENCES

- Akimkin, V. V. 2015, *Astronomy Reports*, 59, 747  
 Armitage, P. J. 2007, *ArXiv Astrophysics e-prints*  
 —. 2011, *ARA&A*, 49, 195  
 —. 2015, *ArXiv e-prints*, arXiv:1509.06382  
 Bai, X.-N. 2011a, *ApJ*, 739, 50  
 —. 2011b, *ApJ*, 739, 51  
 Balbus, S. A., & Hawley, J. F. 1991, *ApJ*, 376, 214  
 Birnstiel, T., Klahr, H., & Ercolano, B. 2012, *A&A*, 539, A148  
 Booth, R. A., & Clarke, C. J. 2016, *MNRAS*, 458, 2676  
 Brauer, F., Dullemond, C. P., & Henning, T. 2008, *A&A*, 480, 859  
 Carballido, A., Matthews, L. S., & Hyde, T. W. 2016, *ApJ*, 823, 80

- Chatterjee, S., & Tan, J. C. 2014, *ApJ*, 780, 53
- Dominik, C., Blum, J., Cuzzi, J. N., & Wurm, G. 2007, *Protostars and Planets V*, 783
- Draine, B. T. 2011, *Physics of the Interstellar and Intergalactic Medium*
- Draine, B. T., & Sutin, B. 1987, *ApJ*, 320, 803
- Dudorov, A. E., & Khaibrakhmanov, S. A. 2014, *Ap&SS*, 352, 103
- Dullemond, C. P., Henning, T., Visser, R., et al. 2007, *A&A*, 473, 457
- Fortov, V. E., Ivlev, A. V., Khrapak, S. A., Khrapak, A. G., & Morfill, G. E. 2005, *Phys. Rep.*, 421, 1
- Ilgner, M. 2012, *A&A*, 538, A124
- Ivlev, A. V., Padovani, M., Galli, D., & Caselli, P. 2015, *ApJ*, 812, 135
- Johansen, A., Blum, J., Tanaka, H., et al. 2014, *Protostars and Planets VI*, 547
- Johansen, A., & Youdin, A. 2007, *ApJ*, 662, 627
- Kim, S.-H., Martin, P. G., & Hendry, P. D. 1994, *ApJ*, 422, 164
- Larsson, M., Geppert, W. D., & Nyman, G. 2012, *Reports on Progress in Physics*, 75, 066901
- Li, H.-B., Goodman, A., Sridharan, T. K., et al. 2014, *Protostars and Planets VI*, 101
- Mathis, J. S., Ruml, W., & Nordsieck, K. H. 1977, *ApJ*, 217, 425
- McKee, C. F. 1989, *ApJ*, 345, 782
- Nishi, R., Nakano, T., & Umebayashi, T. 1991, *ApJ*, 368, 181
- Okuzumi, S. 2009, *ApJ*, 698, 1122
- Okuzumi, S., Tanaka, H., Takeuchi, T., & Sakagami, M.-a. 2011a, *ApJ*, 731, 95
- . 2011b, *ApJ*, 731, 96
- Oppenheimer, M., & Dalgarno, A. 1974, *ApJ*, 192, 29
- Padovani, M., Galli, D., & Glassgold, A. E. 2009, *A&A*, 501, 619
- Pérez, L. M., Chandler, C. J., Isella, A., et al. 2015, *ApJ*, 813, 41
- Perez-Becker, D., & Chiang, E. 2011, *ApJ*, 727, 2
- Pinilla, P., de Boer, J., Benisty, M., et al. 2015, *A&A*, 584, L4
- Sano, T., Miyama, S. M., Umebayashi, T., & Nakano, T. 2000, *ApJ*, 543, 486
- Semenov, D., Wiebe, D., & Henning, T. 2004, *A&A*, 417, 93
- Spitzer, L. 1962, *Physics of Fully Ionized Gases*
- Surville, C., Mayer, L., & Lin, D. N. C. 2016, *ArXiv e-prints*, arXiv:1601.05945
- Testi, L., Birnstiel, T., Ricci, L., et al. 2014, *Protostars and Planets VI*, 339
- Tielens, A. G. G. M. 2005, *The Physics and Chemistry of the Interstellar Medium*
- Turner, N. J., Fromang, S., Gammie, C., et al. 2014, *Protostars and Planets VI*, 411
- Turner, N. J., & Sano, T. 2008, *ApJ*, 679, L131
- Umebayashi, T. 1983, *Progress of Theoretical Physics*, 69, 480
- Umebayashi, T., & Nakano, T. 1990, *MNRAS*, 243, 103
- van der Marel, N., Pinilla, P., Tobin, J., et al. 2015, *ApJ*, 810, L7
- van der Marel, N., van Dishoeck, E. F., Bruderer, S., et al. 2013, *Science*, 340, 1199
- Velikhov, E. P. 1959, *J. Exptl. Theoret. Phys. (USSR)*, 36, 1398
- Weingartner, J. C., & Draine, B. T. 1999, *ApJ*, 517, 292
- . 2001, *ApJ*, 548, 296
- Whipple, E. C. 1981, *Reports on Progress in Physics*, 44, 1197
- Xu, R., & Bai, X.-N. 2016, *ApJ*, 819, 68
- Zhang, K., Bergin, E. A., Blake, G. A., et al. 2016, *ApJ*, 818, L16
- Zhao, B., Caselli, P., Li, Z.-Y., et al. 2016, *MNRAS*, 460, 2050
- Zsom, A., Ormel, C. W., Güttler, C., Blum, J., & Dullemond, C. P. 2010, *A&A*, 513, A57